First-principles studies of MoF_6 absorption on hydroxylated and non-hydroxylated metal oxide surfaces and implications for atomic layer deposition of MoS_2

Matthew Lawson[1], Elton Graugnard[1], and Lan Li*[1,2]

[1]*Micron School of Materials Science and Engineering, Boise State University, Boise, ID 837062*
[2]*Center for Advanced Energy Studies, Idaho Falls, ID 83401*

Abstract

Significant interest in two-dimensional transition metal dichalcogenides has led to numerous experimental studies of their synthesis using scalable vapor phase methods, such as chemical vapor deposition (CVD) and atomic layer deposition (ALD). ALD typically allows lower deposition temperatures, and nucleation of chemical precursors requires reactions with surface functional groups. A common first-principles method used to study ALD modeling is the calculation of activation energy for a proposed reaction pathway. In this work we calculated the partial charge densities, local density of states (LDoS), Bader charge analysis, adsorption energies, and charge density difference using density functional theory (DFT) to investigate the nucleation of MoF_6 on three oxide surfaces, including Al_2O_3, HfO_2, and MgO. Our findings indicate that hydroxyl groups (OH) help lower the reaction barrier during the first half-cycle of MoF_6 and promote the chemisorption of a precursor on the oxide substrates. This discovery is supported by the formation of highly ionic MF_x (M = metal, x = 1, 2, 3) bonds at the oxide surfaces. By comparing surfaces with and without hydroxyl groups, we highlight the importance of surface chemistry.

*Corresponding author

Keywords:

First-Principles Calculations, Atomic Layer Deposition, Transition Metal Dichalcogenides

1. Introduction

Due to their atomic structures and unique properties, there has been tremendous interest in semiconducting two-dimensional (2D) materials, especially transition metal dichalcogenides (TMDs), which have a composition MX_2 (M = transition metal, X = chalcogen), with a range of band gaps[1] and unique properties[1-7]. An interesting feature of certain TMD materials is the shift of electronic bands when transitioning from bulk to monolayer[1, 8]. Specifically, monolayer MoS_2 becomes a direct band gap semiconductor with a gap of 1.8 eV, whereas its bulk phase has an indirect band gap of 1.3 eV[1, 8]. Due to its novel physical and chemical properties, 2D MoS_2 has drawn attention for its wide range of applications[9] such as electrocatalysis[10-13], photocatalysis[14-17], batteries[18-21], biological applications[22-25], sensors[26-31], and electronic devices[1, 32-35].

2D-MoS_2 has been grown via chemical vapor deposition (CVD), but the high substrate temperatures[36-38] and lack of self-limiting growth[39, 40] have prompted further investigations into alternative methods, such as atomic layer deposition (ALD). Unlike more common CVD techniques, the highly reactive precursor gases for ALD are introduced sequentially into the reactor and never mixed simultaneously[41]. This results in two half-reactions created by each precursor species and its respective surface. The reactions are limited by the number of available surface sites. Sequential cycling of the precursors limits the growth during cycles, and results in precise atomic thickness control. In semiconductor device manufacturing, low *k* dielectric materials are used for interconnect or "Back End of the Line" applications. Their low melting temperatures restrict the process temperature to around 400 °C[42]. In CVD of TMDs, the substrate temperature is typically much higher than this upper limit, making it impractical for integration into semiconductor device fabrication[43]. However, ALD can operate at a much lower temperature making it feasible[41].

A number of studies have reported the ALD processes of TMDs, such as MoS_2 and WS_2, using a variety of precursors[44-58]. Most of these processes yield amorphous as-deposited films, which can be crystallized upon annealing. One such process uses MoF_6 and H_2S to grow amorphous MoS_2 at 200 °C[52, 53]. The initial half reaction of this process introduces MoF_6 to an oxide surface (e.g., atomic layer deposited aluminum oxide, Al_2O_3). Critically, this first half reaction controls the nucleation of the film, only forming a three-atom thick monolayer. Complementary to in situ quartz crystal microbalance (QCM) and Fourier transform infrared (FTIR) spectroscopy characterization, density functional theory (DFT) calculations can be employed to gain insight into various reaction pathways that occur during initial ALD growth[59]. Specifically, DFT can not only explore potential reaction pathways efficiently but also investigate precursor-substrate interactions and quantify electron exchange[60, 61]. Here, we report the use of DFT method to investigate the electronic interactions of a single MoF_6 precursor and three surfaces, including Al_2O_3, HfO_2, and MgO. These oxide materials are widely used in the semiconducting industry ranging from optical applications[62], high-*k* gate dielectrics[63], to catalysis[64]. To simulate the surface reactions, the bulk structures of the substrates were cleaved to expose both oxygen and metal atoms in the vacuum. Recent DFT studies on ALD have found that hydroxylated SiO_2 can facilitate MoS_2 growth[65, 66]. Hydroxyl

groups also facilitate ALD of Si[67], Hf[68], ZnO[69], and more[70]. Building from this insight, we explored nucleation reactions on surfaces without hydroxyl groups (non-hydroxylated) and those with hydrogen atoms terminating the oxygen atoms (hydroxylated). The results indicated that hydroxyl groups are crucial for the nucleation of MoS_2 on these oxide surfaces.

2. Methods

We employed DFT calculations using the Vienna Ab initio Simulation Package (VASP)[71] and Perdew-Burke-Enzerhof (PBE)[72] pseudopotentials with the generalized gradient approximation (GGA) exchange correlation functions. Projector-augmented wave (PAW) pseudopotentials were used. In order to improve the accuracy of the calculations, a cut-off energy of 400 eV was chosen, and residual forces were reduced to 0.01 eV/atom. A vacuum greater than 15 Å was introduced to mitigate spurious interactions. The surfaces were cleaved from relaxed bulk structures, and supercells were generated to increase surface area and underwent another full relaxation. A Γ-centered 5x5x1 k-point mesh was implemented on all surfaces during geometry optimization.

Our initial results and cited literature indicated that ALD simulations converged within a reasonable timeframe when both metal and O atoms terminated at the surface, thus the (110), (100), and (100) surfaces for HfO_2 [73], MgO[74-76], and Al_2O_3 [77, 78] respectively were cleaved from their bulk counterparts. Dimensions and images of the relaxed surfaces were generated using the VESTA[79] program, and are provided in the Supplementary Information. The potential reactivities of surfaces with and without hydroxyl groups were compared by calculating partial charge densities. Next, an MoF_6 precursor was introduced at least 5 Å above the surfaces and underwent a full geometry optimization. To investigate the electronic interactions between precursor and surfaces, local density of states (LDoS) was calculated. The rotationally invariant LSDA+U[80] on site coulombic potentials of 4.38 eV and 4.0 eV were included for the Mo and Hf atoms respectively, and a denser 10x10x1 k-point mesh was implemented. To quantify and compare MoF_6 interactions between the hydroxylated and non-hydroxylated surfaces, Bader charge analysis was employed. Bader charge analysis quantifies the degree of chemical interaction between atoms[81], and is a quantitative method that allows us to study the effect of hydroxyl groups on precursor decomposition[60, 61]. Finally, the adsorption energy of the MoF_6 precursor was calculated to determine the degree of physisorption or chemisorption. The adsorption energy (E_{ads}) was calculated, as follows:

$$E_{ads} = E_{total\ system} - E_{surface} - E_{MoF_6}$$

where $E_{total\ system}$ is the total energy of the surface with precursor, $E_{surface}$ is the total energy of a surface, and E_{MoF_6} is the total energy of a single isolated MoF_6 precursor.

3. Results and Discussion

3.1 Surface Reactivity

To explore surface reactivities, the partial charge densities of the initial surfaces were computed. In Figure 1, the partial charge densities are projected along the *a* axis for the non-hydroxylated Al_2O_3, HfO_2, and MgO substrates. The color scale shows charge density integrated for each material from -1 eV to the Fermi energy. This energy range examines the edge states of the valence band, where electrons participate in chemical bonding. The calculated partial charge densities for the non-hydroxylated surfaces demonstrate the chemically stable surfaces. The charge densities are uniform in each surface and localized around the lattice atoms of all three substrates. The contour lines indicate the regions of equal partial charge densities. Our results suggest that the non-hydroxylated surfaces are not highly reactive. They cannot facilitate MoF_6 deposition, because the charge densities are distributed evenly around the atoms.

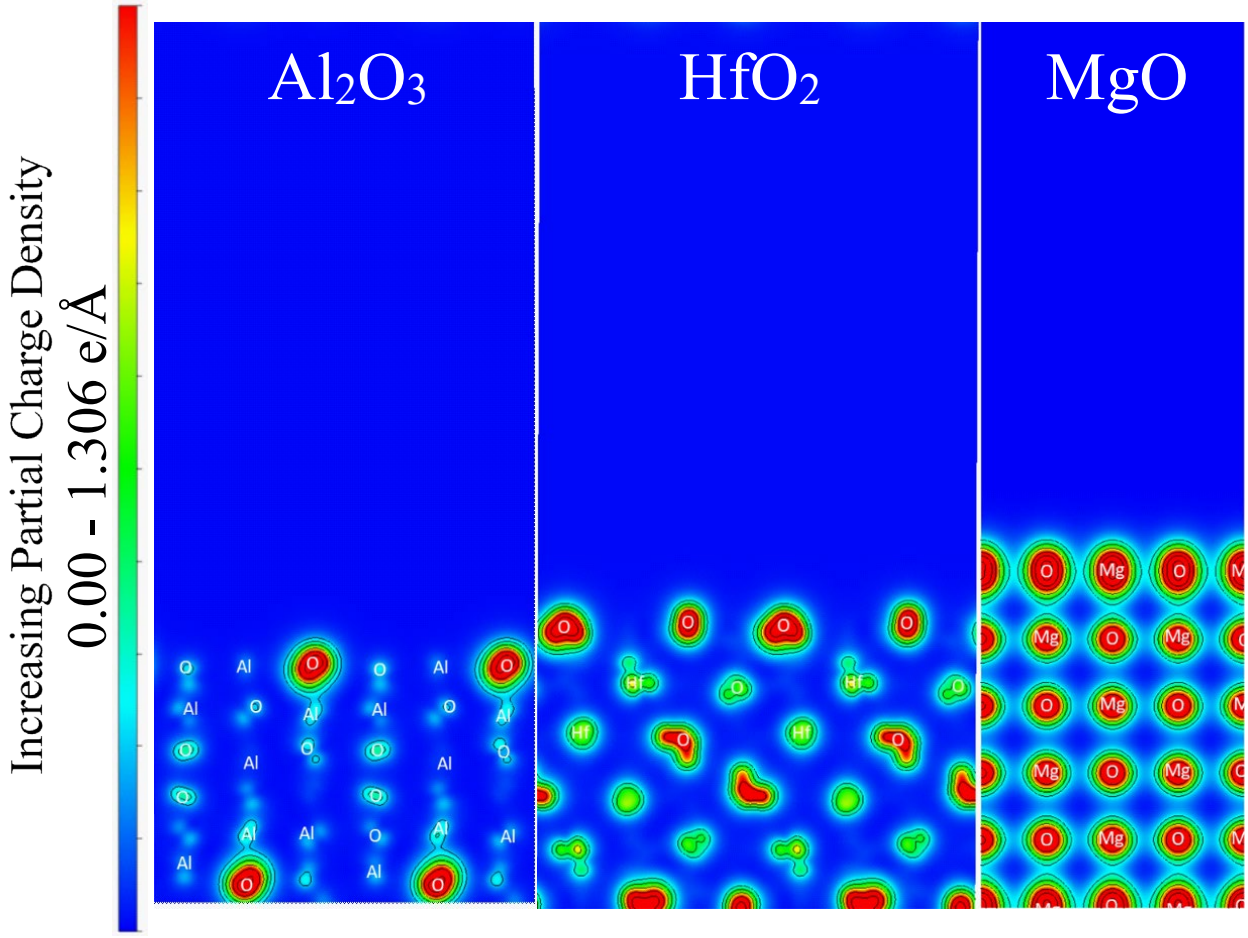

Figure 1. A cross section of the partial charge densities projected along the *a* axis for the non-hydroxylated Al_2O_3, HfO_2, and MgO substrates from -1 eV to the Fermi energy (color online).

Adding hydroxyl groups clearly changes the profile of partial charge densities. Figure 2 plots the partial charge densities along the *a* axis for the hydroxylated Al_2O_3, HfO_2, and MgO substrates from -1 eV to the Fermi energy, where the densities are concentrated at the surfaces. The profile at the surface varies across substrates. The partial charge densities for hydroxylated Al_2O_3 substrate is localized in small "pockets" close to the O atoms at the surface, and the same

phenomenon is observed with the HfO_2 substrate. The electron "pockets" extend to the OH groups, but they are concentrated at the terminating Hf atoms. The partial charge densities for MgO contains a uniform electron cloud extending across the hydroxyl groups at the surface. Our results highlight the importance of the hydroxyl groups, which could redistribute electrons at the surfaces. Hydroxyl groups appear to increase the reactivity of the surface and provide an increase in electron density. Furthermore, the electrons become delocalized, which could promote the chemical bonding of the MoF_6 precursor to the surface.

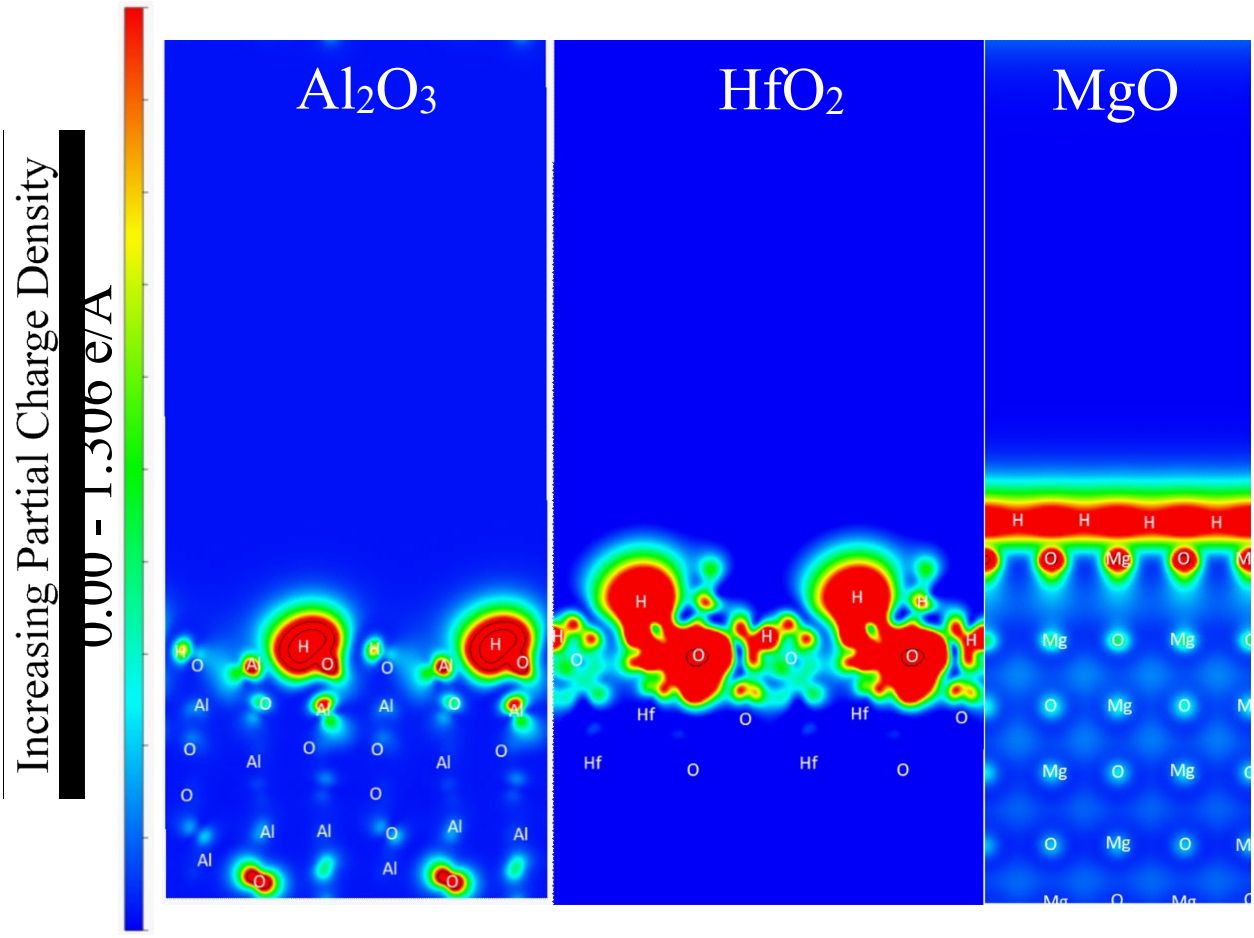

Figure 2. A cross section of the partial charge densities projected along the *a* axis for the hydroxylated Al_2O_3, HfO_2, and MgO substrates from -1 eV to the Fermi energy (color online).

3.2 Precursor Adsorption

To understand the interactions between the non-hydroxylated substrates and the precursor, a single MoF_6 molecule was introduced into the system and underwent a full geometry relaxation. There was no significant structural distortion on any of the surfaces. The LDoS was calculated for each substrate to explore bonding characteristics and electronic interactions. Figure 3 splits the electronic contributions of the surface (in red) and precursor (in blue) for all three non-hydroxylated substrates. The Fermi energy is shifted to 0, and negative energy E states

below the Fermi energy are primarily occupied by the surface. The surfaces do not have overlapping states with the MoF_6 precursor at the Fermi energy. These findings suggest little electronic interaction between the non-hydroxylated surfaces and the MoF_6 precursor. Physisorption is the dominant surface mechanism for the non-hydroxylated surfaces. Later sections will quantify these interactions[82].

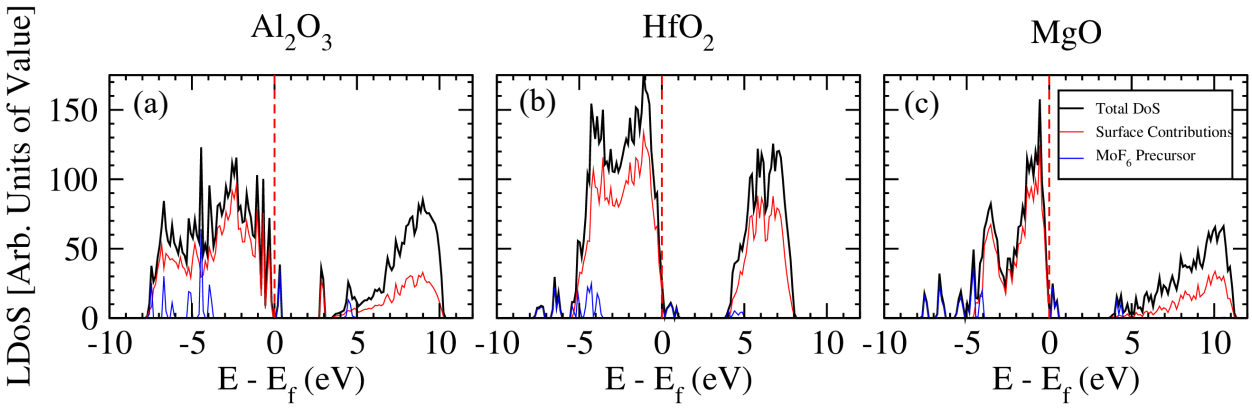

Figure 3. The LDoS for the fully relaxed MoF_6 above the non-hydroxylated (a) Al_2O_3, (b) HfO_2, and (c) MgO substrates. The legend applies to all three substrates.

The partial charge density calculations suggest that the presence of hydroxyl groups enhances the surface reactivity. The LDoS for each hydroxylated substrate with the MoF_6 precursor is plotted in Figure 4, revealing the electronic interactions during deposition. We hypothesized that the electron "pockets" above the hydroxylated Al_2O_3 and HfO_2 substrates in Figure 2 would promote chemical reactions. Figure 4 (a) and (b) show small mid gap states forming below the Fermi energy, and the broadening of the LDoS peaks, which indicates hybridization and chemical bond formation[82]. The hydroxylated MgO substrate in Figure 4 (c) demonstrates similar behavior, however, the MoF_6 precursor creates two small mid gap states, above and below the Fermi energy, at -0.5 and 0.5 eV, and the surface also contributes to these mid gap states.

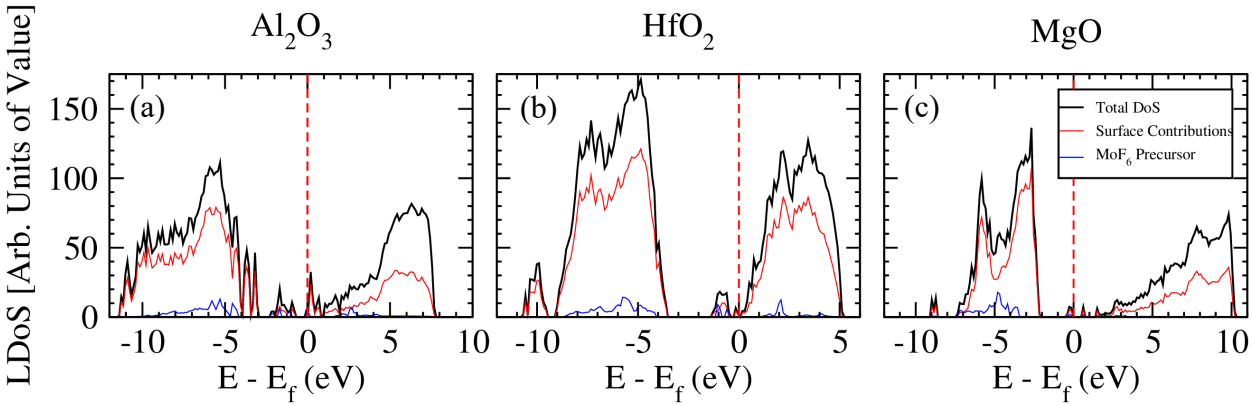

Figure 4. The LDoS for the fully relaxed MoF_6 above the (a) Al_2O_3, (b) HfO_2, and (c) MgO hydroxylated substrates. The legend applies to all three substrates.

In comparison between Figures 3 and 4, the LDoS results for the non-hydroxylated substrates do not show an overlap at the Fermi energy, suggesting no chemical interaction. The LDoS results for the hydroxylated substrates demonstrate the strong surface-precursor interactions stemming from the formation and overlapping of mid gap states. Specifically, Figures 4 (a) and (b) indicate that the surface and precursor both contribute to the states at and near the Fermi energy and show increased bond hybridization, resulting in a strong precursor-surface chemisorption interaction. Figure 4 (c) has fewer overlapping states at the Fermi energy between the surface and precursor. Overall, these mid gap states are derived from the precursor, so further investigation is needed to quantify the physisorption and chemisorption interactions. The LDoS calculations for the non-hydroxylated and hydroxylated substrates reveal two important findings. The first is that non-hydroxylated substrates experience physisorption with the precursor and little electronic interaction. The second is that the hydroxylated surfaces hybridization occurs, leading to chemisorption.

3.3 Electronic Interaction Between Precursor and Surface

The partial charge densities reveal that hydroxylated substrates have an increased surface reactivity and confirm our hypothesis that hydroxyl groups facilitate chemical reactions with MoF_6. The LDoS results suggest precursor-surface physisorption on the non-hydroxylated substrates and precursor-surface chemisorption on the hydroxylated substrates. To better quantify the interactions, we employed Bader charge analysis and calculated the adsorption energies of the precursor on three surfaces. Both can serve as the methods to discern between physical versus chemical interactions as well as quantify the strength of adsorption[81]. Table 1 lists the Bader charge analysis and adsorption energies for the non-hydroxylated and hydroxylated substrates with a single MoF_6 precursor. The Δ Bader is calculated by subtracting the hydroxylated Bader charge values by the non-hydroxylated Bader charge values.

Table 1. The calculated Bader charge analysis for the non-hydroxylated and hydroxylated substrates in presence of a single MoF_6 precursor. A negative Bader charge value means the atomic species is donating valence electrons while a positive value means the atomic species is gaining valence electrons. The adsorption energy of a single MoF_6 precursor E_{ads} is also calculated to quantify the strength of the interaction.

	Al_2O_3			HfO_2			MgO		
	Non-hydroxylated	Hydroxylated		Non-hydroxylated	Hydroxylated		Non-hydroxylated	Hydroxylated	
Atomic Species	**Bader Charge**		***Δ Bader***	**Bader Charge**		***Δ Bader***	**Bader Charge**		***Δ Bader***
Mo	-2.75	-1.53	*1.22*	-2.46	-1.94	*0.51*	-2.44	-2.09	*0.35*
F	0.45	0.70	*0.25*	0.47	0.63	*0.16*	0.44	0.62	*0.18*
F	0.45	0.92	*0.46*	0.42	0.62	*0.20*	0.44	0.62	*0.18*
F	0.46	0.86	*0.40*	0.50	0.70	*0.19*	0.58	0.79	*0.21*
F	0.46	0.85	*0.39*	0.57	0.69	*0.12*	0.53	0.81	*0.28*
F	0.47	0.85	*0.39*	0.47	0.70	*0.23*	0.53	0.79	*0.26*
F	0.45	0.71	*0.25*	0.49	0.72	*0.24*	0.44	0.61	*0.17*
Total F	2.75	4.88	*2.13*	2.93	4.07	*1.14*	2.95	4.24	*1.29*
E_{ads} (eV/MoF_6)	-0.07	-9.95		-0.45	-6.42		-0.57	-20.56	

For complete physisorption we would expect the sum of the Bader charges for the six F atoms from the precursor to be equal to the Bader charge of the central metal Mo atom. Thus, the Mo atom would distribute its available electrons to the surrounding F atoms, and weak van der Waals forces would hold the precursor to the surface. In Table 1, Total F is the sum of the Bader charge for the F atoms from the MoF_6 precursor. The Bader charge for the metal Mo atom is more negative above the non-hydroxylated surfaces than the hydroxylated surface and is equal to the sum Bader charge for the F atoms. These results indicate Mo-F bonds in the precursor are stronger than the chemical bonds formed between the F atoms and the non-hydroxylated surfaces, suggesting physisorption. The opposite trend is observed above the hydroxylated surfaces. The Mo atom above the hydroxylated surface has a less negative Bader charge than the non-hydroxylated surface, and the sum Bader charge for the F atoms also increases. The Mo-F bonds become weaker while the F-surface bonds become stronger, suggesting chemisorption. We attribute the formation of the F-surface bonds due to the electrons contributed by the hydroxylated surfaces.

Chemisorption occurs with the hydroxylated surfaces, because the Bader charge for the F atoms becomes more positive and the metal Mo becomes less negative. To further determine the magnitude of chemisorption, we calculated the adsorption energies in Table 1. The adsorption energy is negative above the non-hydroxylated and hydroxylated surfaces, which implies that for all systems the precursor will be adsorbed to the surface. However, the adsorption energy varies greatly between the non-hydroxylated and hydroxylated surfaces. The adsorption energies for the MoF_6 precursor above the non-hydroxylated surfaces are all less than 0.50 eV/MoF_6. This result, coupled with the LDoS in Figure 3 and Bader charge in Table 1, confirms our hypothesis that physisorption is the dominant mechanism on these non-hydroxylated surfaces. Conversely, the adsorption energies of the MoF_6 precursor above the hydroxylated Al_2O_3, HfO_2, and MgO are -9.95 eV/MoF_6, -6.42 eV/MoF_6, and -20.56 eV/MoF_6, respectively. We attribute the extremely negative adsorption energy for MoF_6 on hydroxylated MgO to the H_2 gas that forms above the surface as seen in SI 4. These significantly more negative adsorption energies, coupled with the

hybridization in the LDoS in Figure 4 and Bader charge analysis in Table 1, indicate chemisorption, caused by the changes in the surface electronic properties in the presence of hydroxyl groups.

To map the location and redistribution of the electron densities, the charge density difference is plotted in Figure 5 for the non-hydroxylated and hydroxylated Al_2O_3 with a single MoF_6 precursor. The charge density difference is calculated using the equation provided in the Supplementary Information and supplies the residual charge density for the electrons contributing upon adsorption. Blue and yellow regions indicate a gain or loss of electrons, respectively. Upon the adsorption of MoF_6, the non-hydroxylated Al_2O_3 reveals an increase in charge density (blue isosurfaces) between the bonds of the Mo-F atoms while there is a decrease in charge density (yellow isosurfaces) at the bonds between the F atoms and surface (Figure 5 (a)). The charge density at the surface redistributes around the surface Al atoms, but it does not appear to participate in bonding. These findings indicate that the non-hydroxylated surface has a weak interaction with an MoF_6 precursor, evidencing that physisorption occurs. The hydroxylated Al_2O_3 surface in Figures 5 (b) shows a sharp contrast in charge density. Upon the adsorption of MoF_6, there is a large increase in the charge density between the surface and F atoms (blue isosurfaces) that extends to the metal Mo atom. This drastic increase in the charge density suggests the covalent bonding characteristics observed during the ALD process. The partial charge density findings are consistent with the HfO_2 and MgO substrates, and those partial charge density plots can be found in the Supplementary Information.

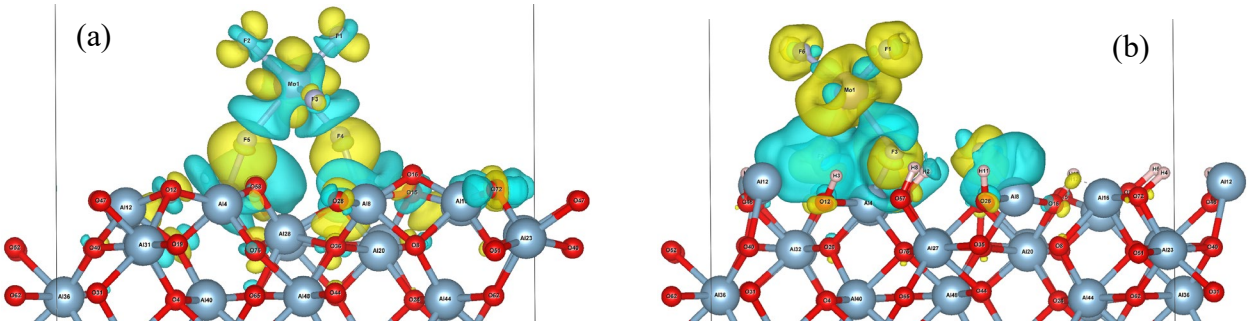

Figure 5. Charge density difference for the non-hydroxylated (a) and hydroxylated (b) Al_2O_3 with MoF_6. The yellow and blue regions indicate a loss and gain of electrons, respectively. The plotted charge density difference highlights the covalent behavior that forms with hydroxylated surfaces.

3.4 Discussions

Our work highlights the importance of hydroxyl groups in consistent with prior DFT works[65, 67-70, 83]. Hydroxyl groups control the first half-cycle for ALD of MoS_2. Treated Al_2O_3, HfO_2, and MgO substrates without hydroxyl groups are less reactive and do not appear to facilitate deposition. Precursor-surface chemisorption is observed on the hydroxylated substrates, but the precursor bonds do not form with the hydroxyl groups. Differences between the oxide surfaces could also play an important role in deposition. While all three oxides have high melting temperatures and large band gaps the crystal structures vary. The highly ionic MgO has a cubic

structure where the valence states of Mg and O are 2^+ and 2^- respectively. The Mg and O exchange electrons and form inherently strong Mg-O bonds. The addition of hydroxyl groups at the surface could break these inherently strong bonds and facilitate deposition. The valence state of HfO_2 is similar to MgO. The valence states of Hf and O are 2^+ and 2^- respectively, but HfO_2 has a distinctly different crystal structure. HfO_2 has a more complicated bonding structure with 7-coordinated Hf atom centers. ALD on HfO_2 could depend on the surface termination due to the number of O atoms, and therefor hydroxyls. The Al_2O_3 substrate has valence states of 3^+ and 2^- for Al and O respectively, which resulted in a different bonding structure. Al_2O_3 was extremely sensitive to the hydroxyl groups, and two F atoms dissociated onto the surface. The 3^+ valence state of Al helped form highly ionic AlF_3.

This work is unique because we identify highly ionic MF_x-surface bonds during the first half cycle of MoF_6. We attribute this to an increase in the electron densities around the Mo atom of the precursor and the surface O atoms which forms chemical bonds. For the MoF_6 precursor, a low operation temperature (i.e., or a high hydroxyl concentration) could result in the ionic MF_x surface bonds that appear to be a driving thermodynamic factor and potentially could control nucleation. Ultimately, Mo-O bonds are present in experimental growth, and they play an important role forming low dimensional MoS_2. We propose that the formation of Mo-O bonds is controlled by the hydroxyl concentration. Hydroxyl groups and their densities can vary surface reactivity and change surface chemistry, leading to a controlling nucleation of ALD. The quality of the grown films is dependent on the choice of substrate. Our computational results indicate that an area-selective ALD can be achieved through surface chemistry modification.

4. Conclusions

We present a comprehensive first-principles study of the substrates with and without hydroxyl groups for ALD of MoS_2 using MoF_6 on Al_2O_3, HfO_2, and MgO. DFT-based methods were used to calculate quantum interactions during the first half-cycle with MoF_6 in order to gain detailed insight into the nucleation process. We studied the precursor and surface interactions by calculating their partial charge densities, LDoS, Bader charge analysis, and adsorption energies. The partial charge densities reveal that the surfaces become more reactive in the presence of hydroxyl groups. The surface composition also affects the partial charge density distribution. The LDoS results demonstrate that the non-hydroxylated surfaces have little to no electronic interactions with the MoF_6 precursor while the hydroxylated surfaces experience some degree of bond hybridization. The Bader charge analysis quantitatively demonstrates that the non-hydroxylated surfaces form a weak interaction with the precursor through physisorption while the hydroxylated surfaces strongly interact with the MoF_6 precursor through chemisorption. Finally, the calculated adsorption energies highlight this difference. Substrates without hydroxyl groups have low adsorption energies of -0.45, -0.57, and -0.07 eV/MoF_6 for HfO_2, MgO, and Al_2O_3, respectively. Coupling these low adsorption energies with their respective LDoS calculations and Bader charge values, we suggest that physisorption is the dominant mechanism on the non-hydroxylated surfaces. Conversely, the adsorption energies of the fully hydroxylated

surfaces increase to -9.95, -6.42, and -20.56 eV/MoF_6 for Al_2O_3, HfO_2, and MgO, respectively. Coupling their respective LDoS calculations, Bader charge values, and adsorption energies with the charge density difference figures, we suggest that chemisorption is the dominant mechanism above hydroxylated surfaces. Our study also highlights the importance of substrate choice and how different substrates react with the precursor, and indicate the potential for area-selective ALD.

Acknowledgments:

This research made use of the resources of the High Performance Computing Center at Idaho National Laboratory, which is supported by the Office of Nuclear Energy of the U.S. Department of Energy and the Nuclear Science User Facilities under Contract No. DE-AC07-05ID14517. We would also like to acknowledge high-performance computing support of the R2 compute cluster (DOI: 10.18122/B2S41H) provided by Boise State University's Research Computing Department. This work was supported in part by an NSF CAREER Grant No. 1751268. We thank Jake Soares, JD Hues, Steve Hues, and Jeffrey Elam for valuable discussions.

5. References

[1] Q.H. Wang, K. Kalantar-Zadeh, A. Kis, J.N. Coleman, M.S. Strano, Electronics and optoelectronics of two-dimensional transition metal dichalcogenides, Nature nanotechnology, 7 (2012) 699.

[2] Y. Gong, J. Lin, X. Wang, G. Shi, S. Lei, Z. Lin, X. Zou, G. Ye, R. Vajtai, B.I. Yakobson, Vertical and in-plane heterostructures from WS2/MoS2 monolayers, Nature materials, 13 (2014) 1135-1142.

[3] W. Huang, X. Luo, C.K. Gan, S.Y. Quek, G. Liang, Theoretical study of thermoelectric properties of few-layer MoS 2 and WSe 2, Physical Chemistry Chemical Physics, 16 (2014) 10866-10874.

[4] X. Gu, R. Yang, Phonon transport in single-layer transition metal dichalcogenides: A first-principles study, Applied Physics Letters, 105 (2014) 131903.

[5] M. Lawson, I. Williamson, Z.-Y. Ong, L. Li, First-principles analysis of structural stability, electronic and phonon transport properties of lateral MoS2-WX2 heterostructures, Computational Condensed Matter, (2019) e00389.

[6] I. Williamson, S. Li, A.C. Hernandez, M. Lawson, Y. Chen, L. Li, Structural, electrical, phonon, and optical properties of Ti-and V-doped two-dimensional MoS 2, Chemical Physics Letters, 674 (2017) 157-163.

[7] I. Williamson, A.C. Hernandez, W. Wong-Ng, L. Li, High-throughput computational screening of electrical and phonon properties of two-dimensional transition metal dichalcogenides, JOM, 68 (2016) 2666-2672.

[8] M. Chhowalla, H.S. Shin, G. Eda, L.-J. Li, K.P. Loh, H. Zhang, The chemistry of two-dimensional layered transition metal dichalcogenide nanosheets, Nature chemistry, 5 (2013) 263.

[9] X. Zhang, Z. Lai, C. Tan, H. Zhang, Solution-Processed Two-Dimensional MoS2 Nanosheets: Preparation, Hybridization, and Applications, Angewandte Chemie International Edition, 55 (2016) 8816-8838.

[10] M.-R. Gao, M.K. Chan, Y. Sun, Edge-terminated molybdenum disulfide with a 9.4-Å interlayer spacing for electrochemical hydrogen production, Nature communications, 6 (2015) 7493.

[11] J. Kibsgaard, Z. Chen, B.N. Reinecke, T.F. Jaramillo, Engineering the surface structure of MoS 2 to preferentially expose active edge sites for electrocatalysis, Nature materials, 11 (2012) 963.

[12] J. Xie, H. Zhang, S. Li, R. Wang, X. Sun, M. Zhou, J. Zhou, X.W. Lou, Y. Xie, Defect-rich MoS2 ultrathin nanosheets with additional active edge sites for enhanced electrocatalytic hydrogen evolution, Advanced materials, 25 (2013) 5807-5813.

[13] S. Xu, D. Li, P. Wu, One-pot, facile, and versatile synthesis of monolayer MoS2/WS2 quantum dots as bioimaging probes and efficient electrocatalysts for hydrogen evolution reaction, Advanced Functional Materials, 25 (2015) 1127-1136.

[14] J. Chen, X.J. Wu, L. Yin, B. Li, X. Hong, Z. Fan, B. Chen, C. Xue, H. Zhang, One-pot synthesis of CdS nanocrystals hybridized with single-layer transition-metal dichalcogenide nanosheets for efficient photocatalytic hydrogen evolution, Angewandte Chemie International Edition, 54 (2015) 1210-1214.

[15] Y. Hou, Z. Wen, S. Cui, X. Guo, J. Chen, Constructing 2D porous graphitic C3N4 nanosheets/nitrogen-doped graphene/layered MoS2 ternary nanojunction with enhanced photoelectrochemical activity, Advanced materials, 25 (2013) 6291-6297.
[16] A.B. Laursen, S. Kegnæs, S. Dahl, I. Chorkendorff, Molybdenum sulfides—efficient and viable materials for electro-and photoelectrocatalytic hydrogen evolution, Energy & Environmental Science, 5 (2012) 5577-5591.
[17] W. Zhou, Z. Yin, Y. Du, X. Huang, Z. Zeng, Z. Fan, H. Liu, J. Wang, H. Zhang, Synthesis of few-layer MoS2 nanosheet-coated TiO2 nanobelt heterostructures for enhanced photocatalytic activities, small, 9 (2013) 140-147.
[18] K. Chang, W. Chen, L-cysteine-assisted synthesis of layered MoS2/graphene composites with excellent electrochemical performances for lithium ion batteries, ACS nano, 5 (2011) 4720-4728.
[19] S. Ding, J.S. Chen, X.W. Lou, Glucose-assisted growth of MoS2 nanosheets on CNT backbone for improved lithium storage properties, Chemistry–A European Journal, 17 (2011) 13142-13145.
[20] Y.X. Wang, S.L. Chou, D. Wexler, H.K. Liu, S.X. Dou, High-Performance Sodium-Ion Batteries and Sodium-Ion Pseudocapacitors Based on MoS2/Graphene Composites, Chemistry–A European Journal, 20 (2014) 9607-9612.
[21] F. Zhou, S. Xin, H.W. Liang, L.T. Song, S.H. Yu, Carbon nanofibers decorated with molybdenum disulfide nanosheets: synergistic lithium storage and enhanced electrochemical performance, Angewandte Chemie International Edition, 53 (2014) 11552-11556.
[22] L. Cheng, J. Liu, X. Gu, H. Gong, X. Shi, T. Liu, C. Wang, X. Wang, G. Liu, H. Xing, PEGylated WS2 nanosheets as a multifunctional theranostic agent for in vivo dual-modal CT/photoacoustic imaging guided photothermal therapy, Advanced materials, 26 (2014) 1886-1893.
[23] S.S. Chou, B. Kaehr, J. Kim, B.M. Foley, M. De, P.E. Hopkins, J. Huang, C.J. Brinker, V.P. Dravid, Chemically exfoliated MoS2 as near-infrared photothermal agents, Angewandte Chemie International Edition, 52 (2013) 4160-4164.
[24] T. Liu, C. Wang, X. Gu, H. Gong, L. Cheng, X. Shi, L. Feng, B. Sun, Z. Liu, Drug delivery with PEGylated MoS2 nano-sheets for combined photothermal and chemotherapy of cancer, Advanced materials, 26 (2014) 3433-3440.
[25] W. Yin, L. Yan, J. Yu, G. Tian, L. Zhou, X. Zheng, X. Zhang, Y. Yong, J. Li, Z. Gu, High-throughput synthesis of single-layer MoS2 nanosheets as a near-infrared photothermal-triggered drug delivery for effective cancer therapy, ACS nano, 8 (2014) 6922-6933.
[26] J.-S. Kim, H.-W. Yoo, H.O. Choi, H.-T. Jung, Tunable volatile organic compounds sensor by using thiolated ligand conjugation on MoS2, Nano letters, 14 (2014) 5941-5947.
[27] F.K. Perkins, A.L. Friedman, E. Cobas, P. Campbell, G. Jernigan, B.T. Jonker, Chemical vapor sensing with monolayer MoS2, Nano letters, 13 (2013) 668-673.
[28] Y. Tan, R. He, C. Cheng, D. Wang, Y. Chen, F. Chen, Polarization-dependent optical absorption of MoS 2 for refractive index sensing, Scientific reports, 4 (2014) 7523.
[29] Z. Yin, H. Li, H. Li, L. Jiang, Y. Shi, Y. Sun, G. Lu, Q. Zhang, X. Chen, H. Zhang, Single-layer MoS2 phototransistors, ACS nano, 6 (2011) 74-80.
[30] Z. Zeng, Z. Yin, X. Huang, H. Li, Q. He, G. Lu, F. Boey, H. Zhang, Single-Layer Semiconducting Nanosheets: High-yield preparation and device fabrication, Angewandte Chemie International Edition, 50 (2011) 11093-11097.

[31] C. Zhu, Z. Zeng, H. Li, F. Li, C. Fan, H. Zhang, Single-layer MoS2-based nanoprobes for homogeneous detection of biomolecules, Journal of the American Chemical Society, 135 (2013) 5998-6001.
[32] R. Ganatra, Q. Zhang, Few-layer MoS2: a promising layered semiconductor, ACS nano, 8 (2014) 4074-4099.
[33] X. Huang, Z. Zeng, H. Zhang, Metal dichalcogenide nanosheets: preparation, properties and applications, Chemical Society Reviews, 42 (2013) 1934-1946.
[34] K. Lee, H.Y. Kim, M. Lotya, J.N. Coleman, G.T. Kim, G.S. Duesberg, Electrical characteristics of molybdenum disulfide flakes produced by liquid exfoliation, Advanced materials, 23 (2011) 4178-4182.
[35] J. Liu, Z. Zeng, X. Cao, G. Lu, L.H. Wang, Q.L. Fan, W. Huang, H. Zhang, Preparation of MoS2-Polyvinylpyrrolidone Nanocomposites for Flexible Nonvolatile Rewritable Memory Devices with Reduced Graphene Oxide Electrodes, Small, 8 (2012) 3517-3522.
[36] Y.H. Lee, X.Q. Zhang, W. Zhang, M.T. Chang, C.T. Lin, K.D. Chang, Y.C. Yu, J.T.W. Wang, C.S. Chang, L.J. Li, Synthesis of large-area MoS2 atomic layers with chemical vapor deposition, Advanced materials, 24 (2012) 2320-2325.
[37] J. Shi, D. Ma, G.-F. Han, Y. Zhang, Q. Ji, T. Gao, J. Sun, X. Song, C. Li, Y. Zhang, Controllable growth and transfer of monolayer MoS2 on Au foils and its potential application in hydrogen evolution reaction, ACS nano, 8 (2014) 10196-10204.
[38] Y. Zhan, Z. Liu, S. Najmaei, P.M. Ajayan, J. Lou, Large-area vapor-phase growth and characterization of MoS2 atomic layers on a SiO2 substrate, Small, 8 (2012) 966-971.
[39] Y.-C. Lin, W. Zhang, J.-K. Huang, K.-K. Liu, Y.-H. Lee, C.-T. Liang, C.-W. Chu, L.-J. Li, Wafer-scale MoS 2 thin layers prepared by MoO 3 sulfurization, Nanoscale, 4 (2012) 6637-6641.
[40] X. Ling, Y.-H. Lee, Y. Lin, W. Fang, L. Yu, M.S. Dresselhaus, J. Kong, Role of the seeding promoter in MoS2 growth by chemical vapor deposition, Nano letters, 14 (2014) 464-472.
[41] S.M. George, Atomic layer deposition: an overview, Chemical reviews, 110 (2009) 111-131.
[42] H. Kim, Atomic layer deposition of metal and nitride thin films: Current research efforts and applications for semiconductor device processing, Journal of Vacuum Science & Technology B: Microelectronics and Nanometer Structures Processing, Measurement, and Phenomena, 21 (2003) 2231-2261.
[43] H.O. Pierson, Handbook of chemical vapor deposition: principles, technology and applications, William Andrew, 1999.
[44] T. Scharf, S. Prasad, M. Dugger, P. Kotula, R. Goeke, R. Grubbs, Growth, structure, and tribological behavior of atomic layer-deposited tungsten disulphide solid lubricant coatings with applications to MEMS, Acta Materialia, 54 (2006) 4731-4743.
[45] T. Scharf, S.V. Prasad, T. Mayer, R. Goeke, M. Dugger, Atomic layer deposition of tungsten disulphide solid lubricant thin films, Journal of materials research, 19 (2004) 3443-3446.
[46] R. Browning, P. Padigi, R. Solanki, D.J. Tweet, P. Schuele, D. Evans, Atomic layer deposition of MoS2 thin films, Materials Research Express, 2 (2015) 035006.
[47] S. Cadot, O. Renault, M. Frégnaux, D. Rouchon, E. Nolot, K. Szeto, C. Thieuleux, L. Veyre, H. Okuno, F. Martin, A novel 2-step ALD route to ultra-thin MoS 2 films on SiO 2 through a surface organometallic intermediate, Nanoscale, 9 (2017) 538-546.

[48] T.A. Ho, C. Bae, S. Lee, M. Kim, J.M. Montero-Moreno, J.H. Park, H. Shin, Edge-on MoS2 thin films by atomic layer deposition for understanding the interplay between the active area and hydrogen evolution reaction, Chemistry of Materials, 29 (2017) 7604-7614.
[49] Y. Jang, S. Yeo, H. Kim, S.-H. Kim, Wafer-scale, conformal and direct growth of MoS2 thin films by atomic layer deposition, Applied Surface Science, 365 (2016) 160-165.
[50] Z. Jin, S. Shin, D.H. Kwon, S.-J. Han, Y.-S. Min, Novel chemical route for atomic layer deposition of MoS 2 thin film on SiO 2/Si substrate, Nanoscale, 6 (2014) 14453-14458.
[51] T. Jurca, M.J. Moody, A. Henning, J.D. Emery, B. Wang, J.M. Tan, T.L. Lohr, L.J. Lauhon, T.J. Marks, Low-Temperature Atomic Layer Deposition of MoS2 Films, Angewandte Chemie International Edition, 56 (2017) 4991-4995.
[52] S. Letourneau, M.J. Young, N.M. Bedford, Y. Ren, A. Yanguas-Gil, A.U. Mane, J.W. Elam, E. Graugnard, Structural Evolution of Molybdenum Disulfide Prepared by Atomic Layer Deposition for Realization of Large Scale Films in Microelectronic Applications, ACS Applied Nano Materials, 1 (2018) 4028-4037.
[53] A.U. Mane, S. Letourneau, D.J. Mandia, J. Liu, J.A. Libera, Y. Lei, Q. Peng, E. Graugnard, J.W. Elam, Atomic layer deposition of molybdenum disulfide films using MoF6 and H2S, Journal of Vacuum Science & Technology A: Vacuum, Surfaces, and Films, 36 (2018) 01A125.
[54] M. Mattinen, T. Hatanpää, T. Sarnet, K. Mizohata, K. Meinander, P.J. King, L. Khriachtchev, J. Räisänen, M. Ritala, M. Leskelä, Atomic layer deposition of crystalline MoS2 thin films: new molybdenum precursor for low-temperature film growth, Advanced Materials Interfaces, 4 (2017) 1700123.
[55] D.K. Nandi, U.K. Sen, D. Choudhury, S. Mitra, S.K. Sarkar, Atomic layer deposited MoS2 as a carbon and binder free anode in Li-ion battery, Electrochimica Acta, 146 (2014) 706-713.
[56] S. Shin, Z. Jin, D.H. Kwon, R. Bose, Y.-S. Min, High turnover frequency of hydrogen evolution reaction on amorphous MoS2 thin film directly grown by atomic layer deposition, Langmuir, 31 (2015) 1196-1202.
[57] L.K. Tan, B. Liu, J.H. Teng, S. Guo, H.Y. Low, K.P. Loh, Atomic layer deposition of a MoS2 film, Nanoscale, 6 (2014) 10584-10588.
[58] A. Valdivia, D.J. Tweet, J.F. Conley Jr, Atomic layer deposition of two dimensional MoS2 on 150 mm substrates, Journal of Vacuum Science & Technology A: Vacuum, Surfaces, and Films, 34 (2016) 021515.
[59] D.E. Simon, Atomic-scale simulation of ALD chemistry, Semiconductor Science and Technology, 27 (2012) 074008.
[60] L. Huang, B. Han, B. Han, A. Derecskei-Kovacs, M. Xiao, X. Lei, M.L. O'Neill, R.M. Pearlstein, H. Chandra, H. Cheng, Density functional theory study on the full ALD process of silicon nitride thin film deposition via BDEAS or BTBAS and NH 3, Physical Chemistry Chemical Physics, 16 (2014) 18501-18512.
[61] J. Radilla, G.E. Negrón-Silva, M. Palomar-Pardavé, M. Romero-Romo, M. Galván, DFT study of the adsorption of the corrosion inhibitor 2-mercaptoimidazole onto Fe (1 0 0) surface, Electrochimica Acta, 112 (2013) 577-586.
[62] S. Shi, S. Qian, X. Hou, J. Mu, J. He, X. Chou, Structural and Optical Properties of Amorphous Al₂O₃ Thin Film Deposited by Atomic Layer Deposition, Advances in Condensed Matter Physics, 2018 (2018) 7598978.
[63] C. Chia, M.M. Shulaker, J. Provine, S.S. Jeffrey, R.T. Howe, ALD HfO2 Films for Defining Microelectrodes for Electrochemical Sensing and Other Applications, ACS applied materials & interfaces, 11 (2019) 26082-26092.

[64] X. Feng, F. Pan, H. Zhao, W. Deng, P. Zhang, H.-C. Zhou, Y. Li, Atomic layer deposition enabled MgO surface coating on porous TiO2 for improved CO2 photoreduction, Applied Catalysis B: Environmental, 238 (2018) 274-283.
[65] M. Shirazi, W. Kessels, A. Bol, Initial stage of atomic layer deposition of 2D-MoS 2 on a SiO 2 surface: A DFT study, Physical Chemistry Chemical Physics, 20 (2018) 16861-16875.
[66] M. Shirazi, W. Kessels, A.A. Bol, Initial stage of atomic layer deposition of 2D-MoS 2 on SiO 2 surface: a DFT study, Physical Chemistry Chemical Physics, (2018).
[67] Y.-C. Jeong, S.-B. Baek, D.-H. Kim, J.-S. Kim, Y.-C. Kim, Initial reaction of silicon precursors with a varying number of dimethylamino ligands on a hydroxyl-terminated silicon (0 0 1) surface, Applied Surface Science, 280 (2013) 207-211.
[68] A.B. Mukhopadhyay, J.F. Sanz, C.B. Musgrave, First-Principles Investigation of Hydroxylated Monoclinic HfO2 Surfaces, Chemistry of Materials, 18 (2006) 3397-3403.
[69] J. Ren, Initial growth mechanism of atomic layer deposition of ZnO on the hydroxylated Si (1 0 0)-2× 1: A density functional theory study, Applied surface science, 255 (2009) 5742-5745.
[70] M. Shirazi, S.D. Elliott, Multiple proton diffusion and film densification in atomic layer deposition modeled by density functional theory, Chemistry of Materials, 25 (2013) 878-889.
[71] G. Kresse, Comput. Matter Sci. 6, 15 (1996);(d) Kresse, G., and Furthmuller, Phys. Rev. B, 54 (1996) 11,169.
[72] J.P. Perdew, K. Burke, M. Ernzerhof, Generalized gradient approximation made simple, Physical review letters, 77 (1996) 3865.
[73] L. LI, Y. LI, X. GUO, Y.-F. ZHANG, W.-K. CHEN, Adsorption and Dissociation of Water on HfO2 (111) and (110) Surfaces, Acta Physico-Chimica Sinica, 29 (2013) 937-945.
[74] F. Eskandari, S. Porter, M. Venkatesan, P. Kameli, K. Rode, J. Coey, Magnetization and anisotropy of cobalt ferrite thin films, Physical Review Materials, 1 (2017) 074413.
[75] H.-J. Freund, N. Nilius, T. Risse, S. Schauermann, A fresh look at an old nano-technology: catalysis, Physical Chemistry Chemical Physics, 16 (2014) 8148-8167.
[76] A.R. Head, J. Schnadt, UHV and Ambient Pressure XPS: Potentials for Mg, MgO, and Mg (OH) 2 Surface Analysis, JOM, 68 (2016) 3070-3077.
[77] J. Handzlik, P. Sautet, Active sites of olefin metathesis on molybdena-alumina system: a periodic DFT study, Journal of Catalysis, 256 (2008) 1-14.
[78] A.S. Sandupatla, K. Alexopoulos, M.-F.o. Reyniers, G.B. Marin, Ab initio investigation of surface chemistry of alumina ALD on hydroxylated γ-alumina surface, The Journal of Physical Chemistry C, 119 (2015) 13050-13061.
[79] K. Momma, F. Izumi, VESTA 3 for three-dimensional visualization of crystal, volumetric and morphology data, Journal of applied crystallography, 44 (2011) 1272-1276.
[80] A. Liechtenstein, V. Anisimov, J. Zaanen, Density-functional theory and strong interactions: Orbital ordering in Mott-Hubbard insulators, Physical Review B, 52 (1995) R5467.
[81] W. Tang, E. Sanville, G. Henkelman, A grid-based Bader analysis algorithm without lattice bias, Journal of Physics: Condensed Matter, 21 (2009) 084204.
[82] M. Scheffler, C. Stampfl, Theory of adsorption on metal substrates, Electronic structure, 2 (2000) 286.
[83] M. Shirazi, W. Kessels, A. Bol, Strategies to facilitate the formation of free standing MoS2 nanolayers on SiO2 surface by atomic layer deposition: A DFT study, APL Materials, 6 (2018) 111107.